Interference between magnetism and surface roughness in coherent soft x-ray scattering

A. Rahmim,* S. Tixier,† and T. Tiedje‡
Department of Physics and Astronomy, University of British Columbia, Vancouver, British Colombia, Canada V6T 1Z1

S. Eisebitt,§ M. Lörgen, R. Scherer, and W. Eberhardt
Institut für Festkörperforschung, FZ-Jülich, 52425 Jülich, Germany

J. Lüning
Stanford Synchrotron Radiation Laboratory, Stanford University, California 94309

A. Scholl
Advanced Light Source, LBNL, Berkeley, California 94720
(Received 13 December 2001; published 6 June 2002)

In coherent soft x-ray scattering from magnetically ordered surfaces there are contributions to the scattering from the magnetic domains, from the surface roughness, and from the diffraction associated with the pinhole aperture used as a coherence filter. In the present work, we explore the interplay between these contributions by analyzing speckle patterns in diffusely scattered x rays from the surface of magnetic thin films. Magnetic contrast from the surface of antiferromagnetically ordered $LaFeO_3$ films is caused by magnetic linear dichroism in resonant x-ray scattering. The samples studied possess two types of domains with their magnetic orientations perpendicular to each other. By tuning the x-ray energy from one of the two Fe-L_3 resonant absorption peaks to the other, the relative amplitudes of the x-ray scattering from the two domains is inverted which results in speckle pattern changes. A theoretical expression is derived for the intensity correlation between the speckle patterns with the magnetic contrast inverted and not inverted. The model is found to be in good agreement with the x-ray-scattering observations and independent measurements of the surface roughness. An analytical expression for the correlation function gives an explicit relation between the change in the speckle pattern and the roughness, and magnetic and aperture scattering. Changes in the speckle pattern are shown to arise from beating of magnetic scattering with the roughness scattering and diffraction from the aperture. The largest effect is found when the surface roughness scatter is comparable in intensity to the magnetic scatter.

DOI: 10.1103/PhysRevB.65.235421 PACS number(s): 61.10.Eq, 75.70.Kw, 75.50.Ee

I. INTRODUCTION

Thin magnetic films are of considerable scientific interest and are key components in magnetic information storage technology.[1] New applications and improvements in device performance rely on a microscopic understanding of the static and dynamic properties of magnetic order in thin films. Difficulties arise due to the lack of appropriate experimental techniques when one tries to image magnetic structures in buried layers under applied field or when trying to observe the dynamics of a magnetic structure on submicron length scales. In this paper we explore the use of resonant coherent x-ray scattering as a probe of the magnetic order in antiferromagnetic thin films.

Antiferromagnetic (AFM) order is particularly difficult to study since no net magnetic moment can be detected when averaging over the unit cell of a solid or surface. However, an antiferromagnetically ordered Mn monolayer was recently imaged with atomic spatial resolution using spin-polarized scanning-tunneling microscopy.[2] Antiferromagnetic order in surfaces can also be imaged by x-ray magnetic linear dichroism (XMLD) spectromicroscopy with lateral size resolution down to 10 nm.[3,4] In the latter work, magnetic contrast comes from the fact that the scattering/absorption cross section under resonant excitation depends on the relative orientation of the electric-field vector of the incident x rays and the AFM axis. More specifically, XMLD is the difference in cross section for x rays polarized perpendicular or parallel to the magnetic moment. In the AFM case the XMLD depends on the expectation value of the square of the local magnetic moment $\langle M^2 \rangle$.[5–7]

An image of antiferromagnetic domains on the surface of a $LaFeO_3$ thin film as measured using photoelectron emission microscopy (PEEM) and exploiting XMLD is shown in Fig. 1. Two types of domains are present with their respective AFM axis perpendicular to each other.[4] The image shows a symmetric domain distribution and an average domain size in the micrometer range. By symmetric we mean that the statistical properties of the two domains are the same.

While XMLD PEEM is valuable as a real-space imaging technique, it has three drawbacks. First, the spatial resolution is limited by the aberrations of the secondary electron imaging system rather than by the wavelength of the incident radiation. Secondly, it is impossible to study the domains in the presence of an applied magnetic field as the secondary electrons interact with the magnetic field. Finally, due to the strong surface sensitivity of techniques based on photoelectrons, buried layers cannot be probed. These drawbacks can be overcome by using x-ray-scattering techniques. For inco-

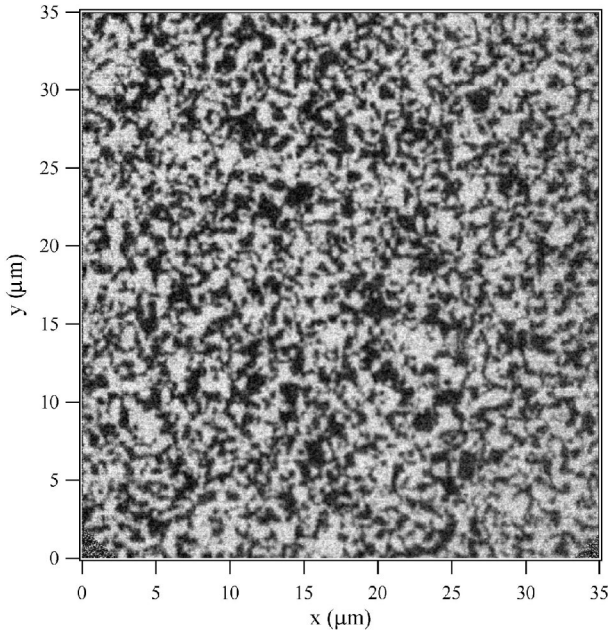

FIG. 1. PEEM image of a $LaFeO_3$ sample showing a symmetric distribution of antiferromagnetic domains (Ref. 4).

herent scattering, use of the spectral dependence of the different scattering channels in order to separate charge and magnetic scattering has been explored in Ref. 8. A coherent soft x-ray scattering experiment which exploits XMLD and shows antiferromagnetic contrast is reported in the present work. Changes in the speckle pattern associated with the magnetic order in $LaFeO_3$ films are observed by tuning the x-ray energy from one of the peaks in the crystal-field multiplet structure at the Fe-L_3 edge to the other. A speckle pattern is observed in the far field when coherent radiation scatters from a surface of a medium with a randomly varying height or refractive index. The resulting pattern is due to interference between waves which undergo various optical path differences or phase shifts after being scattered by different parts of the medium.[9] The speckle manifests itself as a modulation in the intensity of the diffuse scattering provided that the incident radiation is sufficiently coherent. In the x-ray range experimental speckle investigations became feasible with the development of undulators at synchrotron-radiation sources. Coherent hard x-ray scattering experiments demonstrated the potential of the technique in a Bragg reflection geometry.[9,10] Real-space images can be reconstructed from x-ray speckle patterns.[11–13] Coherent x-ray scattering has been used to study magnetic order[14] and observe fluctuations of magnetic domains.[15]

The x-ray scattering from magnetically ordered surfaces contains contributions from the surface roughness and from the magnetic order, if the x-ray wavelength is tuned to a suitable magnetic transition. In addition, the pinhole aperture used as a coherence filter in coherent x-ray scattering contributes a diffraction pattern, which interferes with the diffuse scattering from the surface of the sample. Diffraction from the aperture gives rise to distinct features in coherent experiments. If the aperture is a circular pinhole, Airy rings are present in the scattered intensity and dominate the scat-

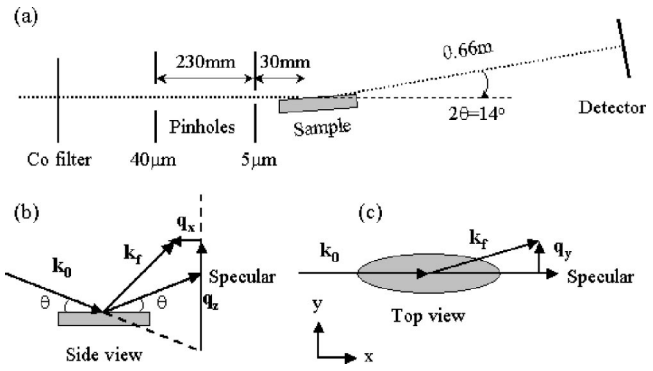

FIG. 2. (a) Experimental setup showing the two-pinhole coherence filter and the grazing incidence geometry. (b) and (c) Definition of the in-plane and out-of-plane momentum transfers q_x, q_y, and q_z, respectively. $\mathbf{k}_f$ and $\mathbf{k}_0$ are the incident and exit scattering vectors. In (b) and (c), the specular direction is also indicated.

tering close to the specularly reflected beam for smooth samples. In the reflection geometry, both the magnetic scattering and the surface-roughness scattering give rise to speckles in the diffuse intensity, with coherent illumination. In this paper we explore the interference between the magnetic scattering, the surface-roughness scattering, and the diffraction from the exit aperture.

An expression is derived for the cross correlation between speckle patterns obtained at two different resonances at the Fe-L_3 edge which have opposite magnetic contrast for the two different orientation antiferromagnetic domains. This expression provides a quantitative measure of the interference between the magnetic scattering, the surface-roughness scattering, and the diffraction from the pinhole.

The experimental setup is described in Sec. II. Coherent scattering data is discussed in Sec. III. The intensity correlation function taking into account magnetic and surface-roughness scattering and diffraction from the pinhole is derived in Sec. IV. A comparison of the theoretical results with the experimental correlation function is discussed in Sec. V.

II. EXPERIMENT

Coherent soft x-ray scattering experiments were performed at the undulator beamline 8.0 of the Advanced Light Source, using a custom-built ultrahigh-vacuum end station. The scattering geometry as well as the definition of the momentum transfers are shown in Fig. 2. The end station consists of a double-pinhole coherence filter, sample manipulator, and a two-dimensional (2D) position sensitive detector for soft x rays consisting of a multichannel plate and resistive anode. Linearly polarized radiation with the electric-field vector perpendicular to the scattering plane entered the end station after being monochromatized ($\lambda/\Delta\lambda \sim 2000$). Measurements were performed at the two peaks at 708.4 eV and 710.2 eV within the Fe-L_3 absorption edge of $LaFeO_3$ using the third undulator harmonic. Stray light from the first harmonic was blocked by a Co transmission filter.

In order to perform a coherent scattering experiment, two conditions need to be fulfilled: (i) the sample has to be illuminated by a laterally coherent beam and (ii) the maximum

path-length difference has to be smaller than the longitudinal coherence length $\xi = \lambda^2/\Delta\lambda \sim 3.5$ μm in our case ($\lambda = 17.5$ Å at 710 eV). In a two-pinhole coherence filter with pinholes of diameters P_1 and P_2 separated by L, condition (i) is fulfilled if $P_2 \leqslant \lambda L/2P_1$.[16,17] In our setup, the arrangement $P_1 = 40$ μm, $P_2 = 5$ μm, and $L = 230$ mm was used, which fulfills this condition and produces a laterally coherent beam behind the second pinhole. The sample is located 30 mm downstream of P_2. The incidence angle of 7° results in an elliptical footprint of the beam on the sample of about 5 μm by 40 μm. The grazing incidence geometry enhances the cross section for the specular and diffuse reflectivities but results in smaller momentum transfers which limit the minimum spatial resolution that can be studied. With this setup and according to condition (ii), the longitudinal coherence is sufficient to observe coherent scattering over the whole detector, and maximum momentum tranfers are ~ 6 μm^{-1} and ~ 100 μm^{-1} for q_x and q_y, respectively. The CsI-coated multichannel plate detector is located 660 mm behind the sample and has an active area of 40-mm width and 20 mm height.

An average coherence length of the incident radiation of ~ 7 μm was determined by fitting the Fraunhofer ring contrast in the experiment (due to scattering from the pinhole P_2) with a calculated Fraunhofer pattern. For this, the measurement was performed without a sample, by placing the detector in the direct beam. The calculation consisted of the convolution of the scattering (Airy pattern) with the Fourier transform of the complex coherence factor.[18]

$LaFeO_3$ films were grown in an oxide molecular-beam epitaxy system by means of a block-by-block growth method on a $SrTiO_3$ (100) substrate.[4,19] The film thickness was 26 nm. The AFM axes of $LaFeO_3$ films made a 45° angle with the sample surface, and assumed only two orientations whose projections on the sample surface were perpendicular to each other.[4]

The samples were imaged by PEEM (Ref. 4) and mounted with one of the AFM axes oriented in the scattering plane. The sample position was not changed during the measurements, so that the illuminated area on the sample remained the same. Atomic force microscopy images of the samples were taken using a Nanoscope IIIa from Digital Instruments.

III. EXPERIMENTAL RESULTS

The calculated x-ray reflectivity spectra for a single domain, for x rays polarized parallel and perpendicular to the AFM axis, are plotted in Fig. 3. The angle of incidence is 7°. The imaginary part of the refractive index was obtained from absorption spectra measured at near normal incidence by PEEM on single domains[4] while the real part was calculated via a Kramers-Kronig transformation. Any dependence of the optical properties on the angle of the incident beam with respect to the surface normal was ignored.[20] With the film thickness at 26 nm, the path length inside the material for an x-ray beam reflected from the substrate-film interface and at the incidence angle of 7° was 426 nm. This neglected the refraction of the x rays at the film-air interface, which would further increase the path length. The nonresonant x-ray-

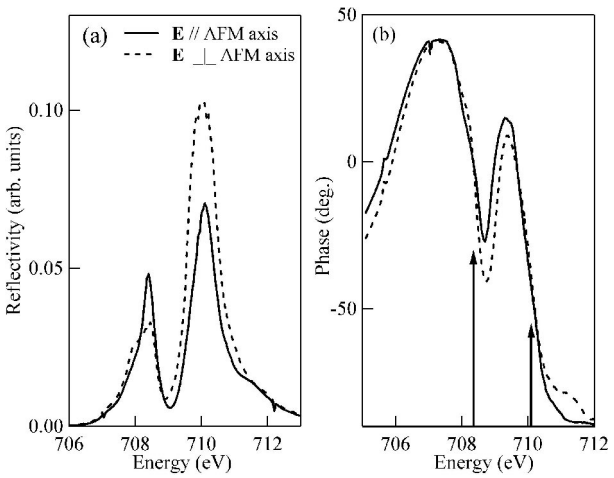

FIG. 3. Calculated soft x-ray reflectivity spectra at 7° incident angle from a $LaFeO_3$ thin film. The modulus (a) and phase (b) of the reflectivity are shown. Note the presence of two resonances at the Fe-L_3 edge and the change in sign of the magnetic contrast when moving from one resonance to the other. At the resonance energies the phase of the reflectivity is identical for both orientations of the incident **E** vector with respect to the AFM axis of the domains.

absorption length at 800 eV was about 200 nm. At the peak of the absorption resonance the absorption length decreased to about 25 nm. Thus x rays that are transmitted into the film are largely absorbed and the back reflection from the substrate-film interface can be neglected. The modulus and phase of the reflectivity are shown in Fig. 3(a) and Fig. 3(b), respectively. Two crystal-field and angular momentum multiplet peaks at the Fe-L_3 edge (708.4 eV and 710.2 eV) are observed. A rather large linear dichroism is seen ($\sim 38\%$), which changes sign when going from one resonance to the other. At the peak in the absorption resonances, the phase of the reflectivity is identical for both orientations of the incident-beam **E** vector with respect to the AFM axis of the domains [Fig. 3(b)]. The magnetic contribution to the resonant x-ray scattering at the peak energies is therefore only due to changes in the amplitude of the reflectivity between the domains and not the phase of the reflectivity.

In Fig. 4, an overview of the scattering from a $LaFeO_3$ surface is shown. The largest intensity is found in the center, corresponding to the specular direction. For better visibility of the diffuse scattering (i.e., outside the specular direction), the color z scale in the image has been saturated in the vicinity of the specular spot where the intensity is largest. Around the center, Fraunhofer diffraction rings are visible (labeled ''A''). Irregularities in the laser-drilled pinhole result in intensity streaks radiating from the central peak. Diffuse scattering from the surface roughness and the AFM domains is observed in the regions outside the Fraunhofer rings and extends at a constant $q = (q_x^2 + q_y^2)^{1/2}$ to form ellipses as shown in the figure. The elliptical shape of the constant q contours is related to the grazing incidence geometry of the experiment. Black spots on the image correspond to dead areas on the CsI-coated multichannel plate detector (labeled ''B''). The near horizontal line (labeled ''C'') in the lower

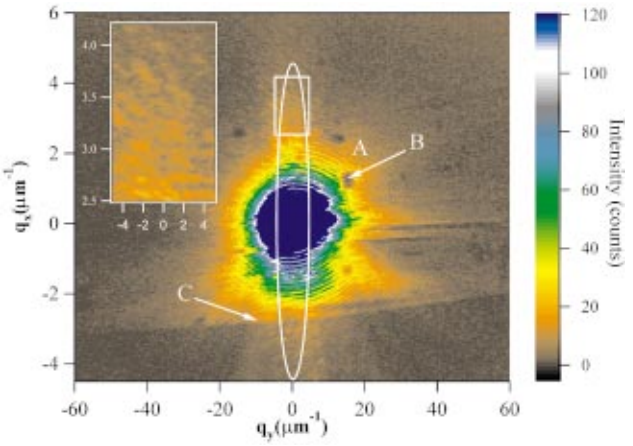

FIG. 4. (Color) Overview of the 2D intensity distribution of the scattered x rays at 710.2 eV from a $LaFeO_3$ surface. The linear *z* false color scale has been purposely saturated in the center. The inset is an expanded view of the speckle dominated region as indicated by the rectangular box. See text for details.

part of the figure is due to the beam footprint intercepting the edge of the sample. Note that Fraunhofer rings are not present below this line while diffuse scattering is still observed. The inset in Fig. 4 is an expanded view of a region away from the Fraunhofer rings as indicated by the rectangular box in Fig. 4. The inset shows speckle due to scattering from the rough surface and from the antiferromagnetic domains. The sizes of the speckle and the spacing between the Fraunhofer rings are solely determined by the wavelength of the radiation used, and by the size of the coherently illuminated area. Speckle (diffuse) scattering dominates over Fraunhofer diffraction at high q_x since the illumination is larger than the typical length scale of the surface roughness and of the magnetic domains.

Speckle pattern changes were observed when changing the photon energy from one of the two peaks of the Fe-L_3 edge (708.4 eV or 710.2 eV) to the other. The changes are only due to magnetic contrast since a 0.25% change in the photon wavelength does not significantly change the roughness scattering contribution to the speckle pattern. This was independently verified by comparing off-resonance data for similar small variations in photon energy.

IV. MAGNETIC INTENSITY CORRELATION FUNCTION

In order to quantify the change in the speckle pattern with a change in energy, a normalized correlation factor γ^{exp} was calculated. For two scattering images covering a given q box and represented by the data matrices M_{hk} and N_{hk} measured at the incident photon energies E_1 and E_2, this figure of merit is defined as

$$\gamma^{exp}(E_1,E_2)=\frac{\sum_{h,k}(M_{hk}-\overline{M}_{hk})(N_{hk}-\overline{N}_{hk})}{\sqrt{\sum_{h,k}(M_{hk}-\overline{M}_{hk})^2\sum_{h,k}(N_{hk}-\overline{N}_{hk})^2}}. \quad (1)$$

The correlation factor is 0 when the images being compared are uncorrelated, 1 when they are perfectly correlated, and -1 when they are perfectly anticorrelated. The subtraction of the mean values ($\overline{M}$, $\overline{N}$) and the normalization in the definition of Eq. (1) permit a direct comparison of position and shape of the speckles, thus canceling the effects of varying total intensity between images and of finite coherence length of the incident radiation (reduced image contrast). Obviously, maximum coherence length is desirable in order to get large speckle contrast in the experiment and therefore maximize the signal-to-noise ratio and minimize the uncertainty in the calculation of γ^{exp}.

Roughness and magnetic scattering both create speckle. Moreover they interfere with each other in the region of q where they have comparable contributions to the scattered intensity. Furthermore, depending on the size of illumination, the pinhole diffraction (Fraunhofer rings) also interferes with the roughness and magnetic scattering. This is particularly well illustrated in Fig. 4 where no speckle is seen in the q_y direction due to dominant pinhole scattering but both pinhole and speckle scattering are seen in the q_x direction. At 7° incident angle, the illumination length is asymptotically eight times shorter in the *y* than in the *x* direction.

In order to study the interference of the pinhole diffraction and the magnetic and roughness scattering, we derive a theoretical expression for the intensity correlation function when the relative reflectivity of the magnetic domains is inverted. Inversion occurs for resonant scattering when there is a 90° rotation of the sample or the incident energy is moved from one of the absorption resonances at the Fe-L_3 edge to the other. We denote the complex scattered amplitude and the scattered intensity from the sample by $A_{\pm}(\mathbf{q})$ and $I_{\pm}(\mathbf{q})$, respectively. The momentum transfer is defined as follows:

$$\mathbf{K}=\mathbf{k}_f-\mathbf{k}_0, \quad (2)$$

where $\mathbf{k}_0$ and $\mathbf{k}_f$ are the ingoing and outgoing wave vectors, respectively. $\mathbf{K}$ is split into its components perpendicular q_z and parallel $\mathbf{q}=(q_x,q_y)$ to the surface.

In order to take the scattering from the magnetic domains into account, we introduce a scattering amplitude factor at resonance $C(\mathbf{x})\exp(i\phi)[1\pm m(\mathbf{x})]$ where $C(\mathbf{x})$ is the product of the aperture function and the modulus of the magnetic scattering amplitude averaged over the two types of domains, ϕ is the phase of the scattering amplitude (the phase is the same for the two domains at the resonances and can therefore be factored out), and $m(\mathbf{x})$ is dimensionless and describes the variation in the modulus of the scattering factor due to the magnetic domains. The sample roughness is described by $h(\mathbf{x})$ which denotes the difference in height between the mean sample height and the height at the lateral coordinate $\mathbf{x}$. Since the 5-μm pinhole is close to the sample (30 mm) we neglect the Fresnel fringes and assume the illumination is uniform over an elliptical area. In the Born approximation and the Fraunhofer limit of scattering, the speckle amplitude is written as the 2D Fourier transform:

$$A_{\pm}(\mathbf{q})=\int C(\mathbf{x})e^{i\phi}[1\pm m(\mathbf{x})]e^{iq_z h(\mathbf{x})}e^{i\mathbf{q}\cdot\mathbf{x}}d\mathbf{x}, \quad (3)$$

where $\mathbf{x}=(x,y)$. The scattered intensity is given by $I_{\pm}(\mathbf{q})=|A_{\pm}(\mathbf{q})|^2$. We introduce the following notation:

$$\Delta A_{\pm}(\mathbf{q})=A_{\pm}(\mathbf{q})-A^0_{\pm}(\mathbf{q}) \tag{4}$$

and

$$\Delta I_{\pm}(\mathbf{q})=I_{\pm}(\mathbf{q})-\langle I_{\pm}(\mathbf{q})\rangle, \tag{5}$$

where

$$A_{0,\pm}(\mathbf{q})=\langle A_{\pm}(\mathbf{q})\rangle \tag{6}$$

with $\langle\ \rangle$ indicating an average over surface roughness and magnetic domain distributions. One must consider ensemble averages in order to derive an analytical expression depending on the statistical properties of the particular surface [e.g., root mean square (rms) roughness, average size of magnetic domains, etc.] and not of the particular configuration of the surface.

Ensemble averages $\langle\ \rangle$ still result in oscillations of the scattered intensity arising from the deterministic contribution of the aperture to the overall scattering (the pinhole gives rise to a characteristic Fraunhofer pattern). In the experimental calculation of the intensity correlation given by Eq. (1), aperture oscillations are smoothed out since the calculation is summed over q space. The q box over which averaging is performed typically covers four Fraunhofer rings. Therefore, in order to assure correspondence between theoretical and experimental calculations of the correlation, we introduce a ''smoothing operator'' $\lfloor\ \rfloor$, which smoothes out aperture oscillations by performing averages in a q box. The normalized magnetic intensity correlation function is then defined in the following way:

$$\gamma(\mathbf{q})=\frac{\lfloor\langle\Delta' I_{+}(\mathbf{q})\Delta' I_{-}(\mathbf{q})\rangle\rfloor}{\sqrt{\lfloor\langle\Delta' I_{+}(\mathbf{q})^2\rangle\rfloor\lfloor\langle\Delta' I_{-}(\mathbf{q})^2\rangle\rfloor}} \tag{7}$$

where

$$\Delta' I_{\pm}(\mathbf{q})=I_{\pm}(\mathbf{q})-\lfloor\langle I_{\pm}(\mathbf{q})\rangle\rfloor. \tag{8}$$

It is important to note that the definition of $\gamma(\mathbf{q})$ suppresses the effects of partial coherence. Partial coherence leads to decreasing contrast in the speckle pattern. It results in the decrease of $\Delta' I_{\pm}(\mathbf{q})$ by a factor $\alpha>1$. However, since both the numerator and denominator in Eq. (7) contain $\Delta' I_{\pm}(\mathbf{q})$, α cancels out and $\gamma(\mathbf{q})$ values stay unchanged.

To better understand the application of the operator $\lfloor\ \rfloor$, we first consider the case of reflection from a flat surface illuminated by a circular pinhole of radius R_0. When incident on the sample at an angle θ (with respect to the sample surface), the illumination forms an ellipse with the elongated axis in the scattering direction given by $R=R_0/\sin(\theta)$. The resulting diffraction pattern (along the q_x direction) is[21]

$$P(q)=P_0\left[\frac{2J_1(qR)}{qR}\right]^2, \tag{9}$$

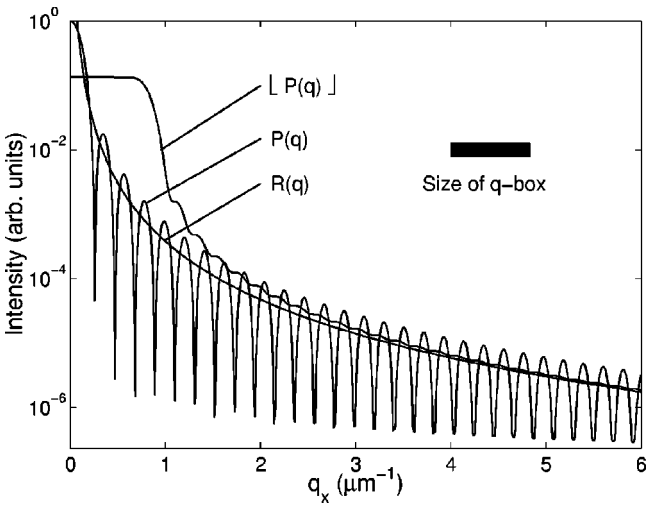

FIG. 5. Average intensity of pinhole scattering as a function of q_x. A circular pinhole of radius $R=2.5$ μm illuminates a flat surface at grazing incidence $\theta=7°$. See text for details.

where P_0 is the peak intensity and J_1 is the Bessel function of the first kind, order one. In the following, $P(q)$ will be referred to as pinhole scattering. In the asymptotic form, one has[22]

$$J_1(x)\sim\sqrt{\frac{2}{\pi x}}\cos\left(x-\frac{3}{4}\right)\pi, \tag{10}$$

which leads to

$$P(q)\sim\frac{8P_0}{\pi(qR)^3}\cos^2\left(qR-\frac{3}{4}\pi\right)$$
$$\sim\frac{4P_0}{\pi}\left[\frac{1}{(qR)^3}+\frac{\cos[2(qR-\frac{3}{4}\pi)]}{(qR)^3}\right] \tag{11}$$

in the asymptotic limit. Note that averaging the second term over a few rings should yield a number close to zero. Thus,

$$R(q)=\frac{4P_0}{\pi(qR)^3} \tag{12}$$

is a very good estimate of $\lfloor P(q)\rfloor$ away from the first few diffraction rings.

$\lfloor P(q)\rfloor$ is plotted in Fig. 5 for a circular pinhole of radius $R=2.5$ μm and at a grazing incidence geometry $\theta=7°$ [$P(q)$ is averaged over a q box extending through about four rings as shown on the graph]. It is seen that $\lfloor P(q)\rfloor$ agrees very well with $R(q)$ after the first few diffraction rings. Trigonometric manipulation gives

$$P(q)^2\sim\frac{16P_0^2}{\pi^2}\left[\frac{3}{2(qR)^6}+\frac{2\cos[2(qR-\frac{3}{4}\pi)]}{(qR)^6}\right.$$
$$\left.+\frac{\cos[4(qR-\frac{3}{4}\pi)]}{2(qR)^6}\right]. \tag{13}$$

Note that after averaging the above expression, the last two terms may be ignored according to the argument given above. Thus we have

$$\lfloor P(q)^2 \rfloor \sim \frac{3}{2}\left[\frac{4P_0}{\pi(qR)^3}\right]^2 = \frac{3}{2}R(q)^2 \tag{14}$$

and

$$\lfloor \Delta' P(\mathbf{q})^2 \rfloor = \lfloor P(q)^2 \rfloor - \lfloor P(q) \rfloor^2 \sim \tfrac{1}{2}R(q)^2. \tag{15}$$

Let us now return to the derivation of the normalized magnetic intensity correlation function. For a symmetric magnetic domain distribution, $\langle \Delta' I_+(\mathbf{q})^2 \rangle = \langle \Delta' I_-(\mathbf{q})^2 \rangle$, thus

$$\gamma(\mathbf{q}) = \frac{\lfloor \langle \Delta' I_+(\mathbf{q}) \Delta' I_-(\mathbf{q}) \rangle \rfloor}{\lfloor \langle \Delta' I_+(\mathbf{q})^2 \rangle \rfloor} \tag{16}$$

since both types of domains contribute equally. The symmetric assumption is used for simplicity in the derivations, however, the results can be trivially extended to the asymmetric case. Combining Eqs. (5) and (8), we obtain

$$\Delta' I_\pm(\mathbf{q}) = \Delta I_\pm(\mathbf{q}) + \beta(\mathbf{q}), \tag{17}$$

where

$$\beta(\mathbf{q}) = \langle I(\mathbf{q}) \rangle - \lfloor \langle I(\mathbf{q}) \rangle \rfloor. \tag{18}$$

Noting that $\beta(\mathbf{q})$ is statistically constant (already ensemble averaged), we get from Eqs. (16) and (18)

$$\gamma(\mathbf{q}) = \frac{\lfloor \langle \Delta I_+(\mathbf{q}) \Delta I_-(\mathbf{q}) \rangle \rfloor + \lfloor \beta(\mathbf{q})^2 \rfloor}{\lfloor \langle \Delta I_+(\mathbf{q})^2 \rangle \rfloor + \lfloor \beta(\mathbf{q})^2 \rfloor}. \tag{19}$$

In Ref. 23, Pederson derived an expression for the spectral speckle correlation. His derivation is extended in the Appendix to the case of magnetic intensity correlation and it is demonstrated that regardless of the sample roughness or magnetic contrast the following relation is valid at $q \gg \pi/2L$ where L is the illumination length:

$$\langle \Delta I_+(\mathbf{q}) \Delta I_\pm(\mathbf{q}) \rangle = |\Gamma_{(+,\pm)}(\mathbf{q})|^2 - |\Gamma^0_{(+,\pm)}(\mathbf{q})|^2, \tag{20}$$

where

$$\Gamma_{(+,\pm)}(\mathbf{q}) = \langle A_+(\mathbf{q}) A^*_\pm(\mathbf{q}) \rangle \tag{21}$$

and

$$\Gamma^0_{(+,\pm)}(\mathbf{q}) = A^0_+(\mathbf{q})(A^0_\pm(\mathbf{q}))^*. \tag{22}$$

The advantage of Eq. (20) is that it expresses intensity correlation functions in terms of amplitude correlation functions, which are easier to evaluate. Note also that

$$\langle I(\mathbf{q}) \rangle = \Gamma_{(+,+)}(\mathbf{q}) = \Gamma_{(-,-)}(\mathbf{q}). \tag{23}$$

Finally, using Eqs. (19) and (20), we get

$$\gamma(\mathbf{q}) = \frac{\lfloor |\Gamma_{(+,-)}(\mathbf{q})|^2 - |\Gamma^0_{(+,-)}(\mathbf{q})|^2 \rfloor + \lfloor \beta(\mathbf{q})^2 \rfloor}{\lfloor |\Gamma_{(+,+)}(\mathbf{q})|^2 - |\Gamma^0_{(+,+)}(\mathbf{q})|^2 \rfloor + \lfloor \beta(\mathbf{q})^2 \rfloor}. \tag{24}$$

In the following, an explicit expression for the above equation is derived.

Equation (21) can be expressed, using Eq. (3),

$$\Gamma_{(+,\pm)}(\mathbf{q}) = \Big\langle \int\int d\mathbf{x_1} d\mathbf{x_2} C(\mathbf{x_1}) C(\mathbf{x_2}) e^{i(\phi_+ - \phi_\pm)} \times [1 + m(\mathbf{x_1})][1 \pm m(\mathbf{x_2})] \times e^{iq_z[h(\mathbf{x_1}) - h(\mathbf{x_2})]} e^{i\mathbf{q}\cdot(\mathbf{x_1} - \mathbf{x_2})} \Big\rangle. \tag{25}$$

At resonance, the phase ($\phi_\pm$) does not depend on the magnetic state as stated earlier, therefore it does not depend on x_1 and x_2. Furthermore, since we are only interested in $|\Gamma_{(+,\pm)}(\mathbf{q})|^2$ in the calculation of Eq. (24), the phase ($\phi_+ - \phi_\pm$) is ignored in the rest of the derivation. Roughness and magnetization are assumed to vary independently, thus the ensemble averages may be taken separately for the roughness and magnetic terms. Under the assumption of Gaussian distributed fluctuations of surface height, and defining $\mathbf{X} = \mathbf{x_1} - \mathbf{x_2}$, we have[24]

$$\langle e^{iq_z[h(\mathbf{x_1}) - h(\mathbf{x_2})]} \rangle = e^{-q_z\sigma^2[1 - \rho_h(\mathbf{X})]}, \tag{26}$$

where σ is the rms roughness and $\rho_h(\mathbf{X})$ is the normalized autocorrelation function of the surface height. Assuming a self-affined surface of fractal dimension $D = 3 - h_r$ with a finite cutoff length for the roughness ξ_h, $\rho_h(\mathbf{X})$ takes the following form:[25,26]

$$\rho_h(\mathbf{X}) = e^{-(X/\xi_h)^{2h_r}}. \tag{27}$$

Such an autocorrelation function is consistent with the power spectral density of our sample surface as measured by atomic force microscopy, as discussed below.

For a symmetric magnetic domain distribution,

$$\langle [1 + m(\mathbf{x_1})][1 \pm m(\mathbf{x_2})] \rangle = 1 \pm \langle m(\mathbf{x_1}) m(\mathbf{x_2}) \rangle = 1 \pm \sigma_m^2 \rho_m(\mathbf{X}), \tag{28}$$

where $\rho_m(\mathbf{X})$ is the normalized magnetic scattering amplitude autocorrelation function and $\sigma_m = \sqrt{\langle m^2 \rangle}$ is the rms magnetic scattering amplitude. Substituting Eqs. (26) and (28) into Eq. (25), we obtain for the amplitude correlation function

$$\Gamma_{(+,\pm)}(\mathbf{q}) = e^{-q_z^2\sigma^2} \int \varrho_c(\mathbf{X})(1 \pm \sigma_m^2 \rho_m(\mathbf{X})) e^{q_z^2\sigma^2\rho_h(\mathbf{X})} e^{i\mathbf{q}\cdot\mathbf{X}} d\mathbf{X}, \tag{29}$$

where

$$\varrho_c(\mathbf{X}) = \int C(\mathbf{x}) C(\mathbf{x} + \mathbf{X}) d\mathbf{x}. \tag{30}$$

Note that by taking $R = |\mathbf{X}|$ and assuming a circular illumination spot on the sample, one may change the variables into polar coordinates, thus expressing Eq. (29) as the *one*-dimensional integral

$$\Gamma_{(+,\pm)}(\mathbf{q}) = e^{-q_z^2\sigma^2} \int \varrho_c(R)(1 \pm \sigma_m^2 \rho_m(R)) \times e^{q_z^2\sigma^2\rho_h(R)} J_0(qR) R dR, \quad (31)$$

where $q = |q_x^2 + q_y^2|^{1/2}$ and J_0 is the Bessel function of the zeroth kind. However, this equation does not hold generally, as the beam input is typically not circular at the surface due to grazing incidence, and therefore integration must be performed separately in both dimensions. Continuing on with Eq. (29),

$$\Gamma_{(+,\pm)}(\mathbf{q}) = e^{-q_z^2\sigma^2} \mathcal{F}_{\mathbf{q}}\{\varrho_c(\mathbf{X})[1 \pm \sigma_m^2 \rho_m(\mathbf{X})] e^{q_z^2\sigma^2\rho_h(\mathbf{X})}\},$$

where $\mathcal{F}_{\mathbf{q}}\{\ \}$ indicates a Fourier transform. Using the convolution theorem, we obtain

$$\Gamma_{(+,\pm)}(\mathbf{q}) = e^{-q_z^2\sigma^2} \mathcal{F}_{\mathbf{q}}\{\varrho_c(\mathbf{X})\} * \mathcal{F}_{\mathbf{q}}\{(1 \pm \sigma_m^2 \rho_m(\mathbf{X})) e^{q_z^2\sigma^2\rho_h(\mathbf{X})}\}, \quad (32)$$

where the asterisk denotes a convolution. It can be rewritten in the form

$$\Gamma_{(+,\pm)}(\mathbf{q}) = e^{-q_z^2\sigma^2} \mathcal{F}_{\mathbf{q}}\{\varrho_c(\mathbf{X})\} * [\mathcal{F}_{\mathbf{q}}\{1\} + \mathcal{F}_{\mathbf{q}}\{e^{q_z^2\sigma^2\rho_h(\mathbf{X})} - 1\} \pm \sigma_m^2 \mathcal{F}_{\mathbf{q}}\{\rho_m(\mathbf{X}) e^{q_z^2\sigma^2\rho_h(\mathbf{X})}\}]. \quad (33)$$

The illumination function $\varrho_c(\mathbf{X})$ is very wide compared to $\rho_h(\mathbf{X})$ and $\rho_m(\mathbf{X})$. Therefore, $\mathcal{F}_{\mathbf{q}}\{\varrho_c(\mathbf{X})\}$ behaves as a delta function when applied to the second and third terms in the bracket expansion of Eq. (33). It thus follows that

$$\Gamma_{(+,\pm)}(\mathbf{q}) = e^{-q_z^2\sigma^2}[P(\mathbf{q}) + H(\mathbf{q}) \pm M(\mathbf{q})], \quad (34)$$

where

$$P(\mathbf{q}) = \mathcal{F}_{\mathbf{q}}\{\varrho_c(\mathbf{X})\}, \quad (35)$$

$$H(\mathbf{q}) = \mathcal{F}_{\mathbf{q}}\{e^{q_z^2\sigma^2\rho_h(\mathbf{X})} - 1\}, \quad (36)$$

$$M(\mathbf{q}) = \sigma_m^2 \mathcal{F}_{\mathbf{q}}\{\rho_m(\mathbf{X}) e^{q_z^2\sigma^2\rho_h(\mathbf{X})}\}. \quad (37)$$

Note that since $\varrho_c(\mathbf{X})$, $\rho_m(\mathbf{X})$, and $\rho_h(\mathbf{X})$ are symmetric, $P(\mathbf{q})$, $M(\mathbf{q})$, and $H(\mathbf{q})$ are real valued.

We can now derive an expression for $\lfloor I(\mathbf{q}) \rfloor$ recalling that the pinhole component of the scattering $P(\mathbf{q})$ must be replaced by an averaged version $\lfloor P(\mathbf{q}) \rfloor$ in order to remove the deterministic aperture oscillations. Since $M(\mathbf{q})$ and $H(\mathbf{q})$ are ensemble-averaged functions, they do not exhibit oscillations. It follows, combining Eqs. (23) and (34), that

$$\lfloor \langle I(\mathbf{q}) \rangle \rfloor = e^{-q_z^2\sigma^2}\{\lfloor P(\mathbf{q}) \rfloor + H(\mathbf{q}) + M(\mathbf{q})\}. \quad (38)$$

Recalling Eq. (18), we get

$$\beta(\mathbf{q}) = P(\mathbf{q}) - \lfloor P(\mathbf{q}) \rfloor = \Delta' P(\mathbf{q}) \quad (39)$$

from which, using Eq. (15), we obtain

$$\lfloor \beta(\mathbf{q})^2 \rfloor = \frac{1}{2} R(\mathbf{q})^2, \quad (40)$$

where

$$R(\mathbf{q}) = \frac{4P_0}{\pi(qR)^3}. \quad (41)$$

Now, combining Eqs. (3) and (6) and assuming a Gaussian distributed roughness and a symmetric magnetic domain distribution, we have

$$A_{\pm}^0(\mathbf{q}) = \int C(x) \langle 1 + m(x) \rangle \langle e^{iq_z h(x)} \rangle e^{i\mathbf{q}\cdot\mathbf{x}} dx = e^{-q_z^2\sigma^2/2} \int C(x) e^{i\mathbf{q}\cdot\mathbf{x}} dx, \quad (42)$$

which, using Eq. (22), leads to

$$\Gamma_{(+,-)}^0(\mathbf{q}) = \Gamma_{(+,+)}^0(\mathbf{q}) = |e^{-q_z^2\sigma^2/2} \mathcal{F}_{\mathbf{q}}(C(x))|^2 = e^{-q_z^2\sigma^2} P(\mathbf{q}), \quad (43)$$

where the convolution theorem was used. Combining Eqs. (24), (34), (40), and (43), we obtain for the magnetic intensity correlation function

$$\gamma(\mathbf{q}) = \frac{\mathcal{M}_- + \frac{1}{2} R(\mathbf{q})^2}{\mathcal{M}_+ + \frac{1}{2} R(\mathbf{q})^2}, \quad (44)$$

where

$$\begin{aligned} \mathcal{M}_{\pm} &= \lfloor (P(\mathbf{q}) + H(\mathbf{q}) \pm M(\mathbf{q}))^2 - P(\mathbf{q})^2 \rfloor \\ &= \lfloor (2P(\mathbf{q}) + H(\mathbf{q}) \pm M(\mathbf{q}))(H(\mathbf{q}) \pm M(\mathbf{q})) \rfloor \\ &= (2R(\mathbf{q}) + H(\mathbf{q}) \pm M(\mathbf{q}))(H(\mathbf{q}) \pm M(\mathbf{q})), \end{aligned} \quad (45)$$

and where we have used the fact that the effect of the "smoothing operator" $\lfloor\ \rfloor$ on the magnetic and roughness terms is negligible. Indeed, these terms are ensemble averaged and do not exhibit short-range oscillations. Combining Eqs. (44) and (45), we get the final result for the magnetic intensity correlation function:

$$\gamma(\mathbf{q}) = \frac{(R(\mathbf{q}) + H(\mathbf{q}) - M(\mathbf{q}))^2 - \frac{1}{2} R(\mathbf{q})^2 + \eta^2}{(R(\mathbf{q}) + H(\mathbf{q}) + M(\mathbf{q}))^2 - \frac{1}{2} R(\mathbf{q})^2 + \eta^2}, \quad (46)$$

where we recall that

$$R(\mathbf{q}) = \frac{4P_0}{\pi(qR)^3}, \quad (47)$$

and where η is a background noise term. Background noise comes from the dark counts in the scattering experiment.

V. COMPARISON OF ANALYTICAL AND EXPERIMENTAL RESULTS

We first make the following observation: it is clear from Eq. (46) that the correlation function $\gamma(\mathbf{q})$ upon inverting the magnetic domain amplitude would be unity if the pinhole

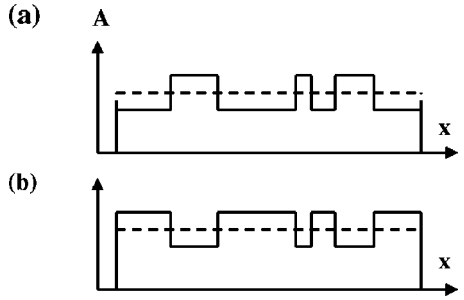

FIG. 6. Schematic of the 1D scattering amplitude (A) from random magnetic domains with a finite illumination region. Inverting the scattering amplitude of the magnetic domains [from (a) to (b)] is equivalent to first inverting the total scattering amplitude and then adding two times the aperture function.

and roughness scatter terms were zero $[R(\mathbf{q})=H(\mathbf{q})=0]$. The importance of the pinhole and roughness scatter can be understood using the schematic shown in Fig. 6. Surface roughness is not included in this example. Inverting the scattering amplitude of the magnetic domains can be mathematically thought of as first inverting the total scattering amplitude and then adding two times the aperture function (Fig. 6). In general the scattered intensity is insensitive to a constant phase offset of the scattering object, therefore the speckle will not change when the magnetic contrast is inverted in an infinite sample. The situation is different for a finite sample as shown in Fig. 6. In this case when the magnetic contrast is inverted, the overall effect on the object cannot be simply described by a phase change, since the aperture function does not invert. Similarly surface-roughness scattering will also remain unaffected by magnetic contrast inversion. Therefore for a finite sample with a rough surface, the interference between the magnetic scattering and the aperture and roughness scattering will produce an overall change in the speckle pattern when the magnetic contrast is inverted.

In order to validate the analytical result [Eq. (46)], we perform a 1D simulation of the correlation function $\gamma(q)$ for a smooth sample with a random magnetic pattern. The pinhole diameter is set equal to 30 μm, the illumination direction is taken to be normal to the surface (i.e., $\theta=90°$), and a relative magnetic scattering amplitude $\sigma_m=0.04$ is assumed. Magnetic domains are artificially created by binning sums of Gaussian functions located randomly on a 1D grid. The full width at half maximum of the Gaussian functions is about 0.15 μm. Correlations $[\gamma^{exp}(q)]$ of the simulated scattering data are calculated according to the definition of Eq. (1). The q box over which averaging is performed is 1.3 $\mu\mathrm{m}^{-1}$. The simulated correlation function $\gamma^{exp}(q)$ is compared to the theoretical calculation of $\gamma(q)$ obtained using Eq. (46). Since the scattering is simulated in one dimension, $R(q)=P_0/2(qR)^2$ is used. The magnetic domain autocorrelation function $\rho_m(X)$ is taken to be $\rho_m(X)=e^{-(X/\xi_m)^2}$ with the parameter $\xi_m=0.115$ μm obtained by fitting $\rho_m(X)$ to the simulated autocorrelation function.

The results are shown in Fig. 7. The simulated and theoretical curves are in good agreement. At small q values (i.e., close to the specular peak) the pinhole scattering dominates and $\gamma(q)\sim 1$. In the higher q limit (i.e., at $q\sim q_m$ where q_m is equal to 2π divided by the size of the domains) the ratio of pinhole to magnetic scattering decreases and beating results in the lowering of the correlation function. In this q range uncorrelated speckle patterns are observed $[\gamma(q)\sim 0]$. As q increases beyond q_m the magnetic scatter decreases faster than the pinhole scatter causing the correlation function to approach unity at high q.

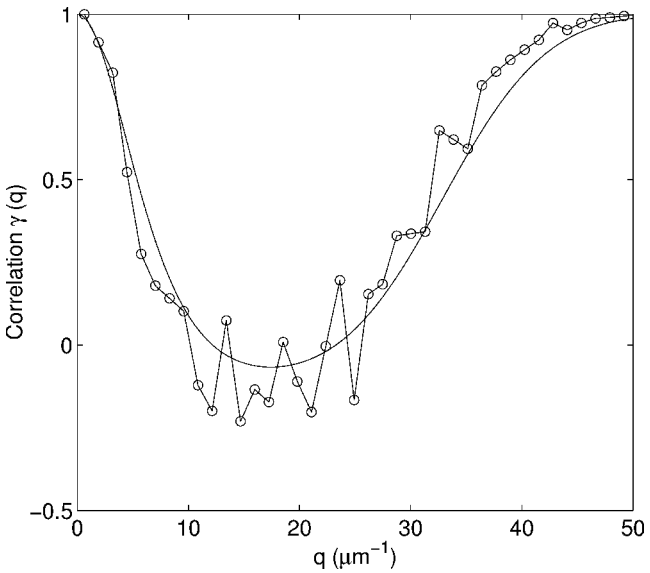

FIG. 7. Comparison of $\gamma^{exp}(q)$ (circles on solid line) calculated from simulated data according to Eq. (1) with the theoretical $\gamma(q)$ (solid line) calculated according to Eq. (46). 1D case.

The quantitative differences exhibited between the two curves are due to the fact that for the calculation of the simulated $\gamma^{exp}(q)$ only one particular sample has been considered, whereas in the calculation of the theoretical $\gamma(q)$, the expression $M(q)$ is found by performing an ensemble average over an infinite number of magnetic domain distributions. This can be directly traced back to definitions of Eq. (1) and Eq. (7), where the latter involves taking both an average over a q range and an ensemble average. An ensemble average is included in the definition of Eq. (7) in order to derive a result that does not depend on a particular surface. The simulated and theoretical curves clearly capture the important feature of the correlation function, namely, it is small in a region of reciprocal space in which the interference between the scattering from the magnetic domains and the diffraction from the pinhole are maximized.

The analytical correlation function [Eq. (46)] does not allow for large negative values of the correlation since both $R(q)$ and $M(q)$ are greater than zero. The minimum value of γ can be easily calculated: $\gamma_{min}=(1-\sqrt{2})/(1+\sqrt{2})\sim -0.17$. The overall scattering is modulated by the deterministic scattering from the aperture. Therefore, the calculation of the correlation according to Eq. (1) where a q box covering several diffraction rings is considered results in mostly positive correlations.

In the remainder of this section, the 2D case and the actual experimental conditions are considered. The autocorre-

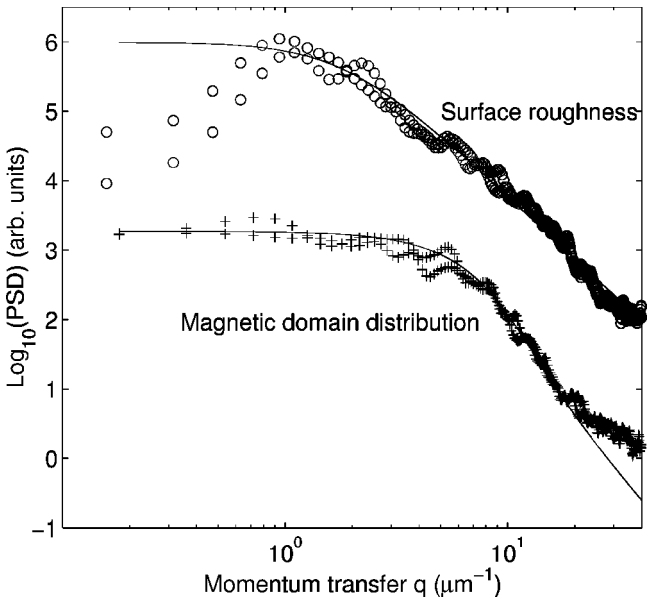

FIG. 8. Experimental power spectral density (PSD) from the surface roughness (top) and from the magnetic domain distribution (bottom). Data has been offset vertically for clarity. The solid lines are theoretical PSD's calculated using exponential correlation functions [Eq. (27)].

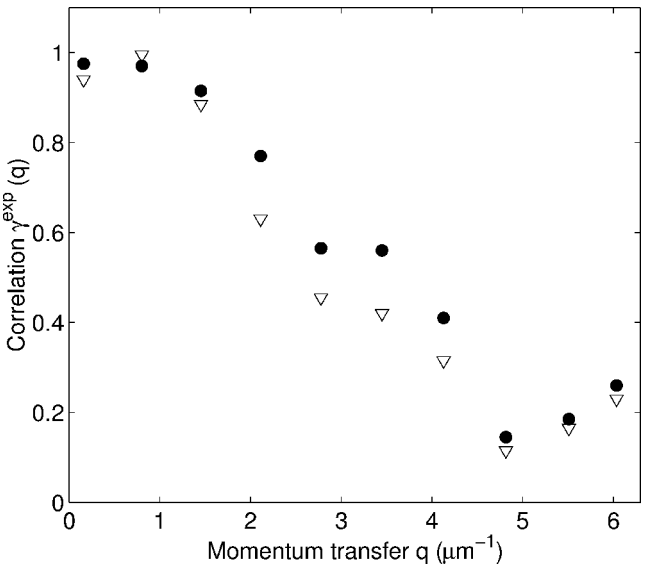

FIG. 9. Experimental correlations γ^{exp} versus momentum transfer q. Solid circles are experimental data, $\gamma^{exp}(E_2,E_2)$, for measurements performed at the same energy but different times, whereas triangles, $\gamma^{exp}(E_1,E_2)$, are for data measured at the two resonances ($E_1=708.4$ eV, $E_2=710.2$ eV).

lation functions of the surface roughness and of the magnetic domains were determined using independent experiments. The sample was measured by atomic force microscopy with image sizes up to 40×40 μm. Parameters for the autocorrelation function ρ_h were obtained by fitting the Fourier transform of ρ_h with the power spectral density (PSD) calculated from the atomic force microscopy data. An identical procedure was followed for the autocorrelation function of the magnetic domains ρ_m using PEEM images. Power spectral densities are shown in Fig. 8 together with the fitted curves. Experimental data are shown in Fig. 8 for two directions on the sample at 90° from each other. The PSD's are found to be isotropic. The surface roughness is well described down to about 1 μm^{-1} using a cutoff length ξ_h of 0.55 μm and a roughness exponent $h_r=0.5$. The rms roughness σ is about 0.3 nm. The magnetic domains are well described using a cutoff length ξ_m of 0.325 μm and an exponent $h_m=0.85$. The rms of the magnetic amplitude σ_m, assuming a 38% change in reflectivity for both domain orientations, is about 0.08 (σ_m is dimensionless). The well-defined corner in the PSD of the magnetic domains followed by a sharp decay ($\sim q^{-3.7}$) indicates that the domains have a well-defined length scale of about 0.65 μm ($2\times\xi_m$).

Experimental values of the correlation as a function of q as calculated according to Eq. (1) are shown in Fig. 9. We calculated γ^{exp} for image areas of $\Delta q_x\sim0.8$ μm$^{-1}\times\Delta q_y\sim5.2$ μm^{-1} in size and for measurements performed either at the same energy but at different times $\gamma^{exp}(E_2,E_2)$ or at different energies and different times $\gamma^{exp}(E_1,E_2)$ ($E_1=708.4$ eV and $E_2=710.2$ eV). The correlation data show a similar trend and decrease with increasing q. This trend is due to the relative increase in noise (which is uncorrelated between measurements) in the images with increasing q. The correlation reaches 0.1 at $q\sim5$ μm^{-1} which indicates that noise dominates the scattering in this q range. Noise is mainly due to low statistics in the diffuse scattering at high q, however in the evaluation of correlations small changes in the illuminated area may also play a role. The correlations $\gamma^{exp}(E_1,E_2)$ are almost always lower than $\gamma^{exp}(E_2,E_2)$ due to changes in the speckle patterns when inverting the magnetic contrast (by tuning the energy from E_1 to E_2).

The experimental values of the correlation are compared in Fig. 10 to theoretical predictions according to Eq. (46). Rather than plotting γ^{exp}, the ratio

$$\gamma_N^{exp}=\gamma^{exp}(E_1,E_2)/\gamma^{exp}(E_2,E_2) \tag{48}$$

of the γ^{exp} values is plotted. This normalized correlation is similar to the correlation of images from which the statistical noise had been subtracted. By statistical noise we mean the shot noise in the measurement of intensities. We assume that the added noise has a zero mean. The correlation γ_N^{exp} has a minimum at around $q=4$ μm^{-1} and approaches unity at high q. The solid line in Fig. 10 is the theoretical curve [Eq. (46)] using the parameters for the autocorrelation functions as obtained by fitting the power spectral densities (Fig. 8). The dashed line is a theoretical prediction using the same parameters as for the solid line but with the addition of the background noise term in Eq. (46). Background noise, which has a constant value in q, is assumed to be comparable in intensity to the roughness scatter at $q=5$ μm^{-1}. The theoretical prediction for the correlation using the experimentally determined surface roughness and magnetic scattering parameters is in good agreement with the experimental results if the background noise is taken into account. Noise and background dominated spectra at high q results in high val-

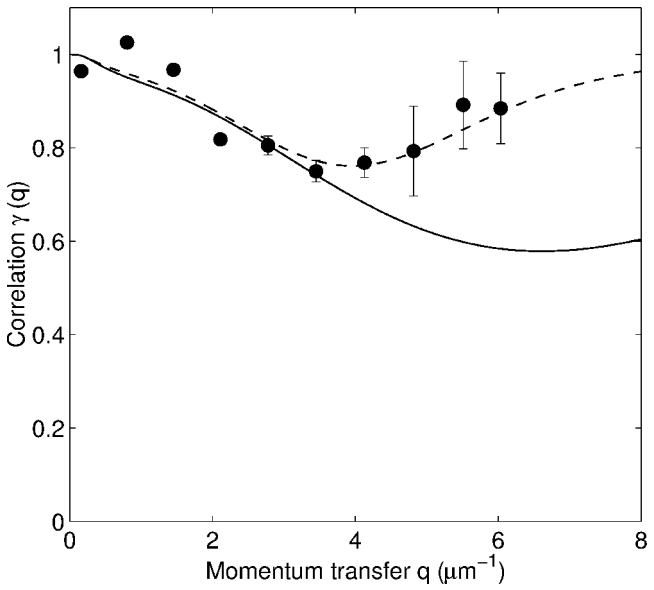

FIG. 10. Correlation γ versus momentum transfer q. Solid circles are experimental data γ_N^{exp} calculated according to Eq. (48). The solid and dashed lines are theoretical predictions $\gamma(q)$ according to atomic force microscopy and PEEM data. Good agreement with the experimental data is obtained by taking the background noise into account (dashed line).

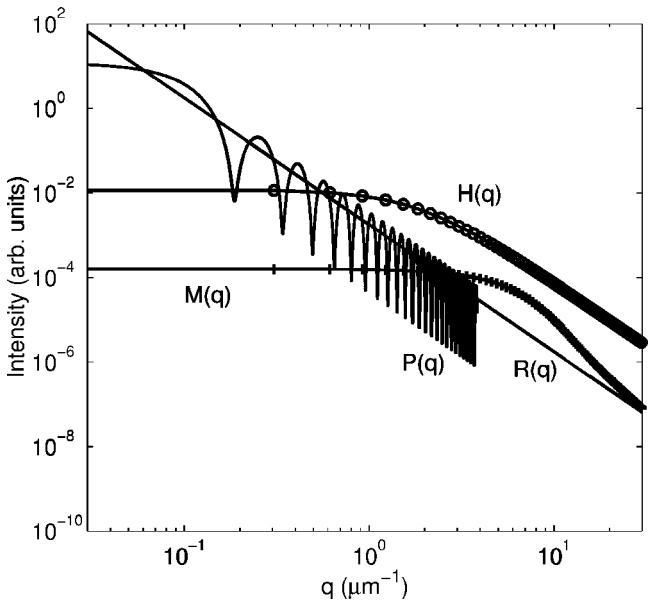

FIG. 11. Momentum-transfer q dependence of the three terms present in Eq. (46) [$R(q)$, $H(q)$, and $M(q)$]. The Fraunhofer diffraction $P(q)$ is also plotted. $P(q)$ is not shown at $q>4$ μm^{-1} since the oscillations cannot be resolved at high q on a logarithmic scale.

ues of the normalized correlation and in a shift of the correlation minimum to lower q values.

The shape of the correlation function versus q can be understood by comparing the three terms $R(q)$, $H(q)$, and $M(q)$ of Eq. (46). Such a comparison is done in Fig. 11 where the fitted parameters are used. At small q, the pinhole scattering $[R(q)]$ dominates and the correlation is unity. As q increases, roughness scattering $H(q)$ becomes increasingly important and eventually dominates. Since the momentum decay at large q of the pinhole and roughness scattering is similar ($\sim q^{-3}$), roughness scattering dominates the entire high q range. The magnetic scattering $M(q)$ is less intense than the roughness scattering over all of the q range. It is closest to $H(q)$ at $q_m \sim 6.5$ μm^{-1} which corresponds to the magnetic domain length scale [sharp corner in $M(q)$]. The correlation is the lowest around q_m (solid line in Fig. 10) where the interference between the roughness and the magnetic scattering is at a maximum. With increasing q, the correlation slowly increases to 1 as the roughness scattering dominates due to its slower decay than the magnetic scattering at high q (the latter decays as $\sim q^{-3.7}$).

The theoretical correlation factor $\gamma(q)$ is plotted in Fig. 12 for different magnetic domain length scales ξ_m [Fig. 12(a)], rms amplitude of the magnetic contrast σ_m [Fig. 12(b)], roughness exponent h_r [Fig. 12(c)], and rms roughness σ [Fig. 12(d)]. The parameters ξ_m, σ_m, h_r and σ range from 0.4 to 1.2 μm, and 0.02 to 0.12, 0.3 to 0.85 and 0.1 to 0.6 nm, respectively. All other parameters are kept constant and identical to the fitted parameters ($\xi_m=0.325$ μm, $\sigma_m=0.08$, $h_m=0.85$, $\xi_h=0.55$ μm, $\sigma=0.3$ nm, and $h_r=0.5$). As one would expect, the increase of ξ_m brings the correlation minimum to lower q values [Fig. 12(a)], and the decrease of the rms amplitude of the magnetic scattering (σ_m) and/or the increase of rms roughness (σ) lead to a smaller dip in the correlation [Figs. 12(b) and 12(d)]. The increase of h_r results in the widening of the correlation dip [Fig. 12(c)]. The faster the decay of the roughness term $H(q)$ at large q, the longer the q range at which beating with the magnetic scatter $M(q)$ is significant. The width of the correlation dip is largest at $h_r=h_m=0.85$ [see Fig. 12(c)]. A similar explanation applies for the change in width of the correlation dip in Fig. 12(a). At larger ξ_m the beating is maximized at q where the decay of the roughness term is slower [close to the corner of $H(q)$] which leads to a smaller width of the correlation dip. The rms roughness is found to have a large influence on the correlation. Given the magnetic contrast of the present experiment, very little magnetic contrast would be measurable if the surface roughness were 1 nm and above (the rms roughness of our sample is 0.3 nm). From Eqs. (36) and (37) and assuming comparable cutoff lengths ξ and autocorrelation exponents h, it appears that $q_z^2\sigma^2$ needs to be comparable to σ_m^2 in order to maximize the beating between $H(q)$ and $M(q)$. In the present experiment, $q_z^2\sigma^2$ is about 0.069 whereas σ_m^2 is 0.0064. A decrease of the rms roughness by a factor of 3, to 0.1 nm (ultrasmooth surface), would result in the maximum beating and to correlation values as low as zero around q_m. The same result would be achieved by decreasing the incident angle to a very small grazing angle, however the latter decrease is limited by the physical dimension of the detector and the momentum range that needs to be explored. In the case of a perfectly smooth surface, beating occurs between the magnetic and the pinhole scattering. Minima in the correlation are found at the crossover points between the two scattering terms. Higher corre-

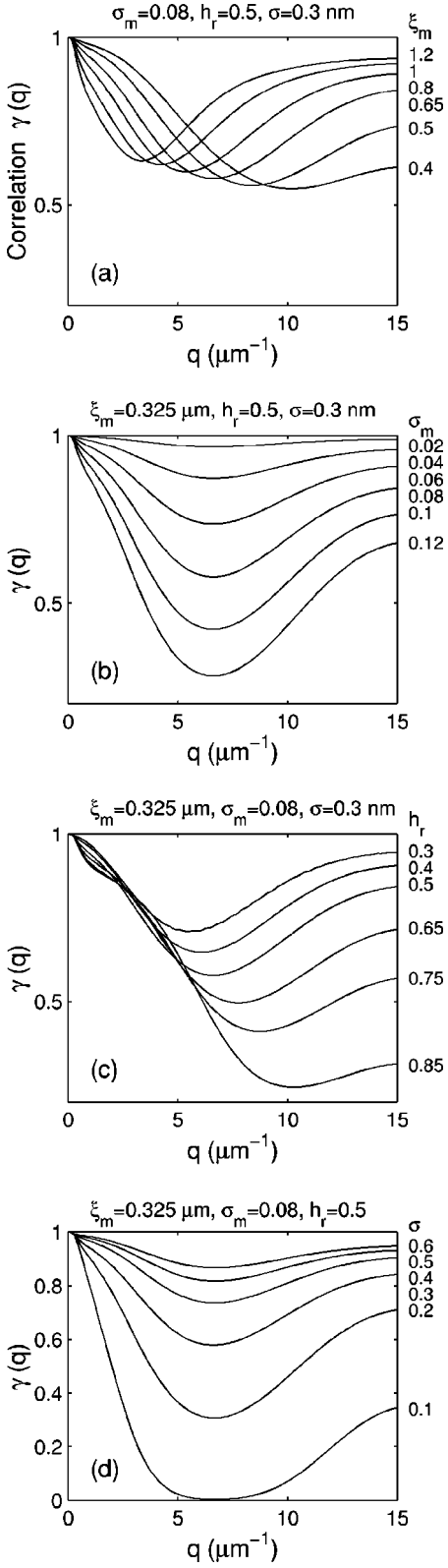

FIG. 12. Theoretical correlation γ versus momentum transfer q for increasing values of (a) magnetic domain length scale ξ_m (μm), (b) rms of the magnetic amplitude σ_m, (c) roughness exponent h_r, and (d) rms roughness σ (nm). All other parameters are kept constant and identical to the fitted parameters ($h_m=0.85$, $\xi_h=0.55$ μm; all other parameters are indicated in the figure panels).

lation values are found away from the crossovers where one of the terms dominates the scattering.

VI. CONCLUSION

We have shown that resonant coherent x-ray scattering is sensitive to antiferromagnetic domain distributions on surfaces due to the x-ray magnetic linear dichroism effect, as long as the surface roughness is very small. Surface-roughness scattering and the x rays diffracted from a pinhole coherence filter interfere with the magnetic scattering. This interference offers, in principle, a method for increasing the sensitivity of the x-ray speckle to magnetic phenomena through the beating of a small magnetic term with the larger diffracted intensity from a pinhole coherence filter, for example. This might be of particular interest in dynamic x-ray scattering experiments,[16] where only the fluctuations of individual speckles are recorded as the dynamics of the system is studied. Especially at high-momentum transfer, such experiments are typically signal limited and additional intensity due to a properly ''designed'' beating may be welcome.

A mathematical expression was developed for the correlation between speckle patterns for two identical magnetic domain distributions but with inverted magnetic scattering contrast. Theoretical predictions were compared with experimental results on $LaFeO_3$. Good agreement was found if background noise, which dominates at high-momentum transfer, is taken into account.

It is found that changes in the speckle pattern upon inverting the scattering amplitude of the magnetic domains (for example, by tuning the x-ray energy) are due to beating of the pinhole and roughness scattering with the magnetic scattering. The largest effect is found when the surface-roughness scatter is comparable in intensity to the magnetic scatter. A detailed understanding of the interplay of the different magnetic and nonmagnetic contributions to the coherent scattering will be important for future experiments attempting a reconstruction of the real-space magnetic domain patterns.

Resonant soft x-ray speckle is a promising tool for studying nanoscale magnetically ordered surfaces and films. It provides information on the structure of the magnetic domains and their time dependence with a spatial and temporal resolution that is limited by the wavelength of the x rays and the x-ray brightness. Unlike electron-based techniques it is insensitive to external magnetic fields, and can probe buried layers.

ACKNOWLEDGMENTS

We thank J. W. Seo, J. Fompeyrine, H. Siegwart, and J-P. Locquet from the IBM research division in Rüschlikon, Switzerland for providing the samples and M. Adamcyk for his help at the beginning of this project. Financial support from the Natural Science and Engineering Research Council of Canada (NSERC) is gratefully acknowledged.

APPENDIX SIMPLIFICATION OF INTENSITY CORRELATION

Pederson[23] has shown for the case of spectral speckle correlation in polychromatic speckle patterns that the intensity correlation may be conveniently expressed in terms of the amplitude correlation. An identical relation is derived here in a more elaborate manner and is shown to be applicable to the case of magnetic intensity correlation in the region where $qL \gg \pi/2$ (L is the size of the sample), regardless of the sample roughness or magnetic contrast. The scattered intensity is given by

$$I_{\pm}(\mathbf{q}) = |A_{\pm}(\mathbf{q})|^2, \tag{A1}$$

where $A_{\pm}(\mathbf{q})$, the complex scattered amplitude, consists of two parts:

$$A_{\pm}(\mathbf{q}) = A^0_{\pm}(\mathbf{q}) + \Delta A_{\pm}(\mathbf{q}), \tag{A2}$$

where $A^0_{\pm}(\mathbf{q}) = \langle A_{\pm}(\mathbf{q}) \rangle$ is the mean scattered amplitude with $\langle\ \rangle$ denoting an ensemble average over surface roughness and magnetic domain distributions, while $\Delta A_{\pm}$ is a fluctuating amplitude component with zero mean. Taking $I_{\pm} = I_{\pm}(\mathbf{q})$, the intensity may now be written

$$I_{\pm} = |A_{\pm}|^2 = |A^0_{\pm} + \Delta A_{\pm}|^2 = I^0_{\pm} + I^d_{\pm} + 2\,\mathrm{Re}\{(A^0_{\pm})^* \Delta A_{\pm}\}, \tag{A3}$$

where we have defined $I^0_{\pm} = |A^0_{\pm}|^2$ and $I^d_{\pm} = |\Delta A_{\pm}|^2$. The mean value is

$$\langle I_{\pm} \rangle = I^0_{\pm} + \langle I^d_{\pm} \rangle \tag{A4}$$

and the fluctuating part is

$$\Delta I_{\pm} = \Delta I^d_{\pm} + 2\,\mathrm{Re}\{(A^0_{\pm})^* \Delta A_{\pm}\}. \tag{A5}$$

The intensity correlation becomes

$$\begin{aligned} \langle \Delta I_+ \Delta I_{\pm} \rangle = {} & \langle \Delta I^d_+ \Delta I^d_{\pm} \rangle + \langle 4\,\mathrm{Re}\{(A^0_+)^* \Delta A_+\} \\ & \times \mathrm{Re}\{(A^0_{\pm})^* \Delta A_{\pm}\} \rangle + 2\,\mathrm{Re}\{\langle \Delta I^d_+ (A^0_{\pm})^* \Delta A_{\pm} \\ & + \Delta I^d_{\pm} (A^0_+)^* \Delta A_+ \rangle\}. \end{aligned} \tag{A6}$$

We are interested in investigating whether $\Delta A_{\pm}$, over an ensemble of input surface roughness and magnetic distributions, exhibits an independent Gaussian distribution of its real and imaginary components with common variance and zero mean (i.e., circular Gaussian statistics). Note that in the literature, it is typically desired for $A_{\pm}$ (not $\Delta A_{\pm}$) to obey circular Gaussian statistics[24] which requires much stronger constraints than in the present case. For ease of demonstration, the roughness is omitted in the rest of the derivations, however, results are easily extendable to the case of rough samples. Assuming that the detector at each point receives contributions from N points on a 1D surface (equally illuminated by the pinhole), the scattered amplitude can be expressed as a 1D discrete Fourier transform:

$$A_{\pm}(q) = \sum_{n=1}^{N} (1 \pm m_n e^{iqL(n/N)}), \tag{A7}$$

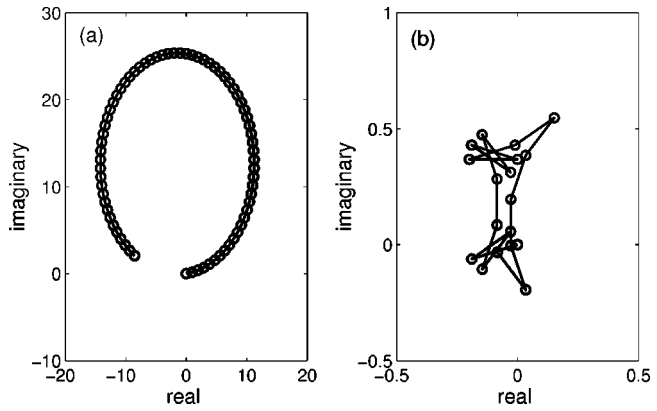

FIG. 13. (a) Pinhole and (b) magnetic contributions from points on an 80-pixel 1D surface, containing 20 randomly generated magnetic domains, at a point on the detector where $qL = 5.6 > \pi/2$ ($|m_n| = 20\%$). Circular Gaussian nature of the magnetic contribution is observed.

where L is the size of the sample, and m_n is as defined in Eq. (3). It follows that

$$\Delta A_{\pm}(q) = \pm \sum_{n=1}^{N} m_n e^{iqL(n/N)}. \tag{A8}$$

Figure 13(a) shows the result of adding the Fourier phase $e^{iqL(n/N)}$ contributions as n ranges from 1 to N.

It is clear that as qL reaches and exceeds a quarter of a full rotation (i.e., $\pi/2$), the pinhole contribution begins to be in both the imaginary and real directions. Figure 13(b) shows the corresponding magnetic contribution to the diffracted amplitude, given by Eq. (A8). In the simulations, domains are generated randomly and they are such that as one moves from one to another, the contribution m_n changes sign ($|m_n| = 20\%$). The figure captures the random-walk nature of $\Delta A_{\pm}(q)$ in both the real and imaginary directions.

It must be kept in mind that we are assuming that the number of magnetic domains in the area of illumination is large, enabling us to make use of the central limit theorem. In regions $qL \gg \pi/2$, therefore, $\Delta A_{\pm}(q)$ will be *circularly* Gaussian distributed over an ensemble of surfaces even though the pinhole contribution $\Sigma_{k=1}^{N} e^{iqL(k/N)}$ may still be completely dominant. On the contrary, this statement would be untrue for $A_{\pm}(q)$ when pinhole scattering, which certainly does not follow Gaussian statistics, is dominant. Note also that the first diffraction minimum occurs at $qL = 2\pi$; therefore, it is correct to assume that $\Delta A_{\pm}$ has independent Gaussian distributed real and imaginary parts with common variance and zero mean beyond the central diffraction ring.

Under the assumption of circular Gaussian statistics for two general random variables B and C, we have the following two properties:[27]

$$\langle \mathrm{Re}\{B\}\mathrm{Re}\{C\} \rangle = \langle \mathrm{Im}\{B\}\mathrm{Im}\{C\} \rangle \tag{A9}$$

and

$$\langle |B|^2 |C|^2 \rangle = \langle |B|^2 \rangle \langle |C|^2 \rangle + |\langle BC^* \rangle|^2. \tag{A10}$$

We now make the observation that the last term in Eq. (A6) contributes zero because it contains only odd powers of $\Delta A_{\pm}$. It also follows from Eq. (A9) that

$$\mathrm{Re}\{\langle \Delta A_{+}(\Delta A_{\pm})^{*}\rangle\} = 2\langle \mathrm{Re}\{\Delta A_{+}\}\mathrm{Re}\{\Delta A_{\pm}\}\rangle. \tag{A11}$$

Therefore, Eq. (A6) may be simplified to the form

$$\langle \Delta I_{+}\Delta I_{\pm}\rangle = \langle \Delta I_{+}^{d}\Delta I_{\pm}^{d}\rangle + \langle 2\,\mathrm{Re}\{(A_{+}^{0})^{*}A_{\pm}^{0}\langle \Delta A_{+}(\Delta A_{\pm})^{*}\rangle\}. \tag{A12}$$

Furthermore, it follows from Eq. (A10) that

$$\langle \Delta I_{+}^{d}\Delta I_{\pm}^{d}\rangle = |\Gamma_{(+,\pm)}^{d}|^{2}, \tag{A13}$$

where we have introduced the correlation function

$$\Gamma_{(+,\pm)}^{d} = \langle \Delta A_{+}\Delta A_{\pm}^{*}\rangle \tag{A14}$$

of the fluctuating component of the scattered amplitude. Upon the introduction of two other correlation functions

$$\Gamma_{(+,\pm)}^{0} = A_{+}^{0}(A_{\pm}^{0})^{*}, \tag{A15}$$

$$\Gamma_{(+,\pm)} = \langle A_{+}A_{\pm}^{*}\rangle = \Gamma_{(+,\pm)}^{0} + \Gamma_{(+,\pm)}^{d} \tag{A16}$$

we arrive at an equation for the intensity correlation:

$$\begin{aligned}\langle \Delta I_{+}\Delta I_{\pm}\rangle &= |\Gamma_{(+,\pm)}^{d}|^{2} + 2\,\mathrm{Re}\{(\Gamma_{(+,\pm)}^{0})^{*}\Gamma_{(+,\pm)}^{d}\} \\ &= |\Gamma_{(+,\pm)}|^{2} - |\Gamma_{(+,\pm)}^{0}|^{2}\end{aligned} \tag{A17}$$

as quoted in Eq. (20).

*Email address: rahmim@physics.ubc.ca
†Email address: tixier@physics.ubc.ca; web address: http://www.physics.ubc.ca/~mbelab/
‡Also at the Department of Electrical and Computer Engineering, University of British Columbia, Vancouver, British Columbia, Canada V6T 1Z1.
§Present address: SSRL, Stanford University, CA 94309.

[1] J.B. Kortright, D.D. Awschalom, J. Stöhr, S.D. Bader, Y.U. Idzerda, S.S.P. Parkin, Ivan K. Schuller, and H.-C. Siegmann, J. Magn. Magn. Mater. **207**, 7 (1999).
[2] S. Heinze, M. Bode, A. Kubetzka, O. Pietzsch, X. Nie, S. Blügel, and R. Wiesendanger, Science **288**, 5472 (2000); **288**, 1805 (2000).
[3] J. Stöhr, A. Scholl, T.J. Regan, S. Anders, J. Lüning, M.R. Scheinfein, H.A. Padmore, and R.L. White, Phys. Rev. Lett. **83**, 1862 (1999).
[4] A. Scholl, J. Stöhr, J. Lüning, J.W. Seo, J. Fompeyrine, H. Siegwart, J.-P Locquet, F. Nolting, S. Anders, E.E. Fullerton, M.R. Scheinfein, and H.A. Padmore, Science **287**, 1014 (2000).
[5] B.T. Thole, G. van der Laan, and G.A. Sawatzky, Phys. Rev. Lett. **55**, 2086 (1985).
[6] J.P. Hannon, G.T. Trammell, M. Blume, and D. Gibbs, Phys. Rev. Lett. **61**, 1245 (1988).
[7] S.W. Lovesey and S.P. Collins, *X-Ray Scattering and Absorption by Magnetic Materials* (Clarendon, Oxford, 1996).
[8] J.B. Kortright, S.K. Kim, G.P. Denbeaux, G. Zeltzer, K. Takano, and E.E. Fullerton, Phys. Rev. B **64**, 092401 (2001).
[9] Z.H. Cai, B. Lai, W.B. Yun, I. McNulty, K.G. Huang, and T.P. Russell, Phys. Rev. Lett. **73**, 82 (1994).
[10] M. Sutton, S.G.J. Mochrie, T. Greytak, S.E. Nagler, L.E. Berman, G.A. Held, and G.B. Stephenson, Nature (London) **352**, 608 (1991).
[11] I.A. Vartanyants, J.A. Pitney, J.L. Libbert, and I.K. Robinson, Phys. Rev. B **55**, 13 193 (1997).
[12] J. Miao, P. Charalambous, J. Kirz, and D. Sayre, Nature (London) **400**, 342 (1999).
[13] I.K. Robinson, J.L. Libbert, I.A. Vartanyants, J.A. Pitney, D.M. Smilgies, D.L. Abernathy, and G. Grübel, Phys. Rev. B **60**, 9965 (1999).
[14] B. Hu, P. Geissbuhler, L. Sorensen, S.D. Kevan, J.B. Kortright, and E.E. Fullerton, Synchrotron Radiat. News **14**, 11 (2001).
[15] F. Yakhou, A. Lëtoublon, F. Livet, M. de Boissieu, and F. Bley, J. Magn. Magn. Mater. **233**, 119 (2001).
[16] A.C. Price, L.B. Sorensen, S.D. Kevan, J. Toner, A. Poniewierski, and R. Holyst, Phys. Rev. Lett. **82**, 755 (1999).
[17] D. Attwood, *Soft X-Rays and Extended Ultraviolet Radiation: Principles and Applications* (Cambridge University Press, Cambridge, England, 1999).
[18] J.W. Goodman, *Statistical Optics* (Wiley, New York, 2000).
[19] J.P. Locquet, J. Perret, J. Fompeyrine, E. Mächler, J.W. Seo, and G. Van Tendeloo, Nature (London) **394**, 453 (1998).
[20] J.B. Kortright and S.-K. Kim, Phys. Rev. B **62**, 12 216 (2000).
[21] J. Matthews and R.L. Walker, *Mathematical Methods of Physics* (Benjamin, New York, 1964).
[22] M. Abramowitz and I.A. Stegun, *Handbook of Mathematical Functions* (Dover, New York, 1964).
[23] H.M. Pederson, Opt. Acta **22**, 15 (1975).
[24] J.W. Goodman, *Laser Speckle and Related Phenomena*, edited by J.C. Dainty (Springer-Verlag, New York, 1975).
[25] S.K. Sinha, E.B. Sirota, S. Garoff, and H.B. Stanley, Phys. Rev. B **38**, 2297 (1988).
[26] S.K. Sinha, Acta Phys. Pol. A **89**, 219 (1996).
[27] L. Mandel, *Progress in Optics*, edited by E. Wolf (North-Holland, Amsterdam, 1963), Vol. 2.